Study of the near wake of a wind turbine in ABL flow using the actuator line method

J Nathan[1], M Bautista[1], C Masson[1] and L Dufresne[1]

[1]Department of Mechanical Engineering, École Technologie Supérieure, 1100 rue Notre-Dame Ouest, Montréal H3C 1K3, QC, Canada

E-mail: joern.nathan.1@ens.etsmtl.ca

Abstract. The main goal of this study is the comparison of the near wake generated by an actuator line immersed in three different flows. A hybrid RANS-LES method is used to analyze the behaviour of the near wake in an atmospheric boundary layer. Then these results are compared to two idealized flow situations commonly found in the literature, such as irrotational flow and homogenous isotropic turbulence. In order to achieve this, a validation of the homogenous isotropic turbulence is conducted. The simulation results and the generated turbulence are compared with respect to the turbulence intensity and the integral length scale of the flow field. Finally to visualise the impact of the different flow conditions on the near wake of a wind turbine, the mean velocities, Reynolds stresses and energy spectra are compared.

1. Introduction

Wind turbine wakes play an essential role in the design of wind farms. They have a significant impact on the energy output and the blades of the downstream turbines. Despite of their importance, they are not yet fully understood. Hence this study focuses on the characterization of the wake of a wind turbine immersed in an atmospheric boundary layer (ABL) flow. The zone of interest is the near wake, where the structure of the helicoidal tip vortices created by the rotating blades are still clearly noticeable. This zone can extend up to two rotor diameter downstream of the turbine [1] [2], hence the present study focuses on this region.

In order to conduct this study, three cases are set up. The first case has an irrotational inflow and represents a wind flow with zero turbulence intensity (TI). The second case exhibits a homogeneous isotropic turbulence, therefore it has a uniform turbulence intensity greater than zero. The third case represents an ABL flow, thus a sheared, turbulent flow. The results on the third case are used as a reference, hence its bulk velocity at the rotor plane U_b is imposed in the first and second cases. Also its mean turbulence intensity is used for generating the turbulence field for the second case. The examined turbine will be the NREL 5MW reference turbine [3].

First there is a brief discussion on the models used: the actuator line method, synthetic turbulence, and a hybrid turbulence method for modelling the ABL. Afterwards the numerical concepts and case details are elaborated and the results are shown. Finally a short conclusion and suggestions for future work are summarized.

2. Modelling concepts

For a LES simulation of the wind flow around the wind turbine the filtered incompressible Navier-Stokes equations in cartesian coordinates are used

$$\frac{\partial \overline{u}_i}{\partial t} + \overline{u}_j \frac{\partial \overline{u}_i}{\partial x_j} = -\frac{1}{\rho}\frac{\partial \overline{p}}{\partial x_i} + \frac{\partial}{\partial x_j}\left[(\nu + \nu_t)\left(\frac{\partial \overline{u}_i}{\partial x_j} + \frac{\partial \overline{u}_j}{\partial x_i}\right)\right] + \frac{F_i}{\rho} \tag{1}$$

$$\frac{\partial \overline{u}_i}{\partial x_i} = 0 \tag{2}$$

whereas the turbulence effects are modelled by a turbulent eddy viscosity ν_t, and F_i/ρ can represent any external forcing (i.e. driving pressure-gradient, turbine forces, Coriolis force, etc.). The closure is achieved by the classic Smagorinsky model with a constant model coefficient C_S of 0.167 in the first two cases and by a hybrid method in the third case (described in subsection 2.3).

2.1. Actuator line method

In order to represent the effect of the rotating blades in the near wake, the actuator line method [4] is chosen. Hereby the forces associated with the rotating blades are calculated by means of the velocity at the blade point without the blade induced component and the airfoil data such as the lift and drag coefficient for a specific Reynolds number and angle of attack. In order to avoid spurious oscillations in the numerical solution when introducing a discrete jump in the source term F_i/ρ in Equation (1), a three dimensional Gaussian distribution

$$\mathcal{G}(r) = \frac{1}{\sigma^3\sqrt{\pi^3}} e^{-\left(\frac{r}{\sigma}\right)^2} \tag{3}$$

is used where r is the distance from the point of the force and the point inside the Gaussian "blob". The standard deviation σ is set to be $2\Delta x$ as compromise between velocity oscillations and the regularization of the forces [5]. The smallest cell size Δx is found in the vicinity of the rotor as described later and it corresponds to $D/22$ for all three cases with D representing the rotor diameter.

2.2. Homogeneous isotropic turbulence

A synthetic velocity field representing homogeneous isotropic turbulence based on the von-Kármán energy spectrum

$$E(k) = CL^{5/3}\frac{L^4k^4}{(1+L^2k^2)^{17/6}} \tag{4}$$

is obtained by using the Mann algorithm[6]. The one-point u-spectrum is given as

$$F_{uu,k}(k_1) = CL^{5/3}\frac{1}{(1+L^2k_1^2)^{5/6}} \tag{5}$$

with C as an arbitrary constant since the resulting velocity field is scaled in order to match the desired turbulence intensity. The length scale L can be used as tuning parameter for obtaining the desired integral length scale $\mathcal{L}$ and k_1 is the wavenumber in the streamwise direction. The implementation used here was presented in [7] and adapted by its authors to produce homogeneous isotropic turbulence.

Table 1. Turbulence model constants.

$k-\omega$ SST constants for ABL flows [11]:					
$\beta_1 = 0.0236$	$\beta_2 = 0.0276$	$\kappa = 0.40$	$\sigma_{k1} = 0.85$	$\sigma_{k2} = 1.0$	$\beta_* = 0.03$
$\sigma_{\omega 1} = 0.5$	$\sigma_{\omega 2} = 0.67$	$a_1 = 0.31$	$\gamma_1 = 0.3255$	$\gamma_2 = 0.3011$	$c_1 = 10.0$
SIDDES constants [10] [12]:					
$C_{k-\epsilon} = 0.61$	$C_{k-\omega} = 0.78$	$C_w = 0.15$	$C_{dt1} = 20.0$	$C_{dt2} = 3.0$	$C_l = 5.0$
$C_t = 1.87$					

2.3. Hybrid turbulence model

The computational cost for an accurate LES simulation close the a solid surface can be rather high. Hybrid turbulence models have been developed to try to alleviate those computational constraints. The hybrid model in this work is based on the Detached Eddy-Simulation (DES) approach. It uses a RANS model to solve the flow in the vicinity of the wall, while a LES approach is used to model the rest of the flow behaviour.

The filtered Navier-Stokes equations (1) and (2) are also employed. In the RANS regions, the term $\overline{u}_i$ represents the time-average velocity, while in the LES regions this term refers to the filtered velocity [8]. The pressure term is treated in the same manner. Additionally ν_t represents the turbulent viscosity or the subfilter viscosity in the RANS and LES regions respectively.

The hybrid model employs the specific turbulent kinetic energy k and the specific dissipation rate $\omega = \varepsilon/(\beta_* k)$ equations of the RANS model $k-\omega$ SST [9][1]. However, the dissipation term ε in the k equation is expressed as $k^{3/2}/\tilde{l}$ to introduce a universal length scale $\tilde{l} = k^{1/2}/(\beta_*\omega)$. The resulting closure equations are [10]

$$\frac{\partial k}{\partial t} + \frac{\partial \overline{u}_j k}{\partial x_j} - \frac{\partial}{\partial x_j}\left[(\nu + \sigma_k \nu_t)\frac{\partial k}{\partial x_j}\right] = P_k - \frac{k^{3/2}}{\tilde{l}} \tag{6}$$

$$\frac{\partial \omega}{\partial t} + \frac{\partial \overline{u}_j \omega}{\partial x_j} - \frac{\partial}{\partial x_j}\left[(\nu + \sigma_\omega \nu_t)\frac{\partial \omega}{\partial x_j}\right] = \frac{\gamma}{\nu_t}P_k - \beta\omega^2 + 2(1-F_1)\frac{\sigma_{\omega 2}}{\omega}\frac{\partial k}{\partial x_j}\frac{\partial \omega}{\partial x_j} \tag{7}$$

Finally the eddy-viscosity is determined by

$$\nu_t = \frac{a_1 k}{\max(\mathrm{a}_1\omega, \mathcal{S}\mathrm{F}_2)}. \tag{8}$$

regardless if it is a RANS or a LES zone being solved. Here $\mathcal{S} = \sqrt{S_{ij}S_{ij}}$ is the characteristic strain rate, P_k is the production term, and F_1 and F_2 are blending functions. Also a_1, β, γ, σ_k and σ_ω are model constants. These constants, collectively represented as ϕ, are calculated by $\phi = F_1\phi_1 + (1-F_1)\phi_2$. Table 1 summarizes all the required constants for the proposed model.

The local value of $\tilde{l}$ regulates if the k and ω equations are solved in RANS or LES mode. This universal length scale $\tilde{l}$ is a function of the RANS and LES length scales, which are defined as

$$l_{RANS} = \frac{\sqrt{k}}{\beta_*\omega} \qquad l_{LES} = C_{DES}\Delta \tag{9}$$

[1] As mention in *http://turbmodels.larc.nasa.gov/sst.html* a typographical error exists in the turbulent dissipation equation (Eq. 1) of this article. Future references use the corrected equation (e.g. [10]).

(from [12] and [13] respectively). Additionally

$$C_{DES} = (1 - F_1)C_{k-\epsilon} + F_1 C_{k-\omega} \tag{10}$$

where β_* and F_1 are the model constant and the blending function from $k-\omega$ SST respectively, and Δ is the filter width [12]. For the DES model, the universal length scale is defined as $\Delta_{DES} = \min(l_{RANS}, l_{LES})$. This turbulence model exhibits two important drawbacks for certain type of simulations. The first issue named grid-induced separation arises for certain type of grids [14]; while the log-layer mismatch (LLM) issue originates when the model is used as a wall-modelled LES [15]. It is important to mention that the LLM mismatch is particularly problematic for all ABL simulations. For this reason the Simplified Improved Delayed Detached Eddy-Simulation (SIDDES) model, which is an enhanced version of DES, is used for this analysis. The SIDDES length scale is defined as

$$\tilde{l}_{SIDDES} = \tilde{f}_d \, l_{RANS} + (1 - \tilde{f}_d) l_{LES} \tag{11}$$

where $\tilde{f}_d$ is an empirical delay function, which together with the definition of $\Delta_{SIDDES} = \min[\max(\mathrm{C_w d_w}, \mathrm{C_w h_{max}}, \mathrm{h_{wn}}), \mathrm{h_{max}}]$ corrects for the LLM. Here, $h_{\max}$ is the maximum edge length of the cell, d_w is the distance to the nearest wall and h_{wn} is the grid step in the wall normal direction [16]. A more detailed explanation about our implementation of the hybrid model is not relevant for the objectives of this work.[2]

Using the $k-\omega$ SST-SIDDES model, for the first two cases its somewhat delicate since the definition of Δ_{SIDDES} is based on a distance to a non-existent solid wall. Consequently, the $k-\omega$ SST-DES was studied. DES was anticipated to be a good candidate for simulating the first two cases because its length scale does not depend on the distance to a solid wall, and no log-layer mismatch is expected. Nevertheless the lack of turbulent content (on the irrotational flow case) poses another challenge for those types of hybrid models. It has been established that the lack of turbulent content in a hybrid model should automatically reduce the simulation to a pure RANS solution [16]. On the other hand, it has been shown that certain hybrid simulation without turbulent content do not always reduce to a RANS solution [15].

The uniform irrotational flow case was analyzed using $k-\omega$ SST-DES. Yet, it was observed that this simulation did not yield the same result as a pure RANS solution. Due to these particular disadvantages, it was thought that Smagorinsky proves to be a more robust model for the first two mentioned cases. However, since it has been shown that the hybrid model presents a "Smagorinsky-like" behaviour [2] the direct comparison of the wakes resulting from the three cases is well-founded.

3. Numerical method

3.1. Framework

The study is realized within the open-source framework OpenFOAM[3] together with the SOWFA[4] project, which contains an implementation of the ALM as described in [5]. A more detailed explanation for the implementation of the method can be found in [17]. The hybrid turbulence model was implemented by the authors.

[2] A thorough explanation will be submitted by M. Bautista et al. as "A hybrid model adapted for wind energy applications. Flat terrain analysis." in the near future

[3] Copyright 2004-2013 OpenCFD Ltd (ESI Group), version 2.2.2.

[4] NWTC Design Codes (SOWFA by Matt Churchfield and Sang Lee) http://wind.nrel.gov/designcodes/simulators/SOWFA/.

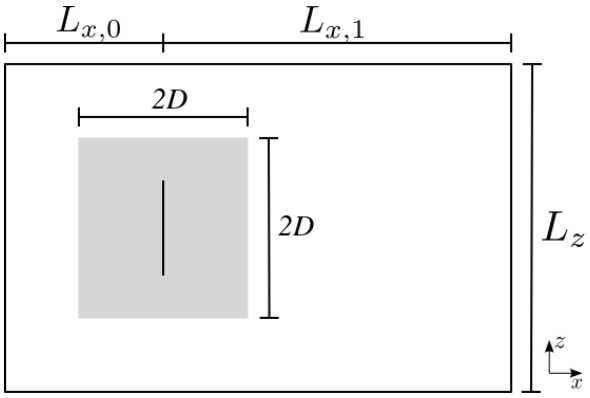

Figure 1. Mesh for case 1 & 2

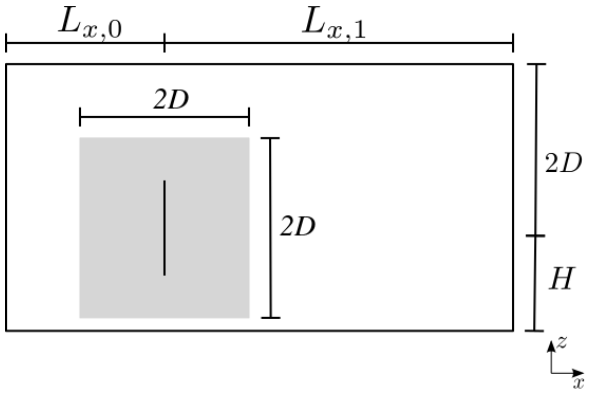

Figure 2. Mesh for case 3

3.2. Case setup

Since the first two cases represent a free stream flow, their meshes are identical. The overall dimensions are $L_{x,0} = 2D$ upstream and $L_{x,1} = 6D$ downstream of the rotor plane, while the lateral extents are $L_y = L_z = 4D$ in each direction as shown schematically in Figure 1. Cubical cells are used in the vicinity of the rotor within a cubical volume with a edge length $2D$ centred at the hub (grey box in Figure 1 and Figure 2). The cells are stretched towards the boundaries, by keeping the highest aspect ratio, occurring near the outlet, under a value of 10.

In order to simulate the ABL on the third case, the bottom region of the domain is reduced to the hub height H and a cell stretching is applied to obtain a recommended dimensionless wall distance $z^+ = u^* z/\nu \leq 1$ [18] with a friction velocity u^* and a molecular viscosity ν. For this reason, very high aspect ratio cells are created close to the ground. This is the price to pay when using a hybrid model with $k-\omega$ SST for simulating an ABL flow. By examining the results of the third case a $z^+ \approx 0.8$ is obtained.

To make the three cases comparable, the same Reynolds number is chosen with $Re_D = U_b D/\nu$, whereas U_b is the bulk velocity in the rotor plane. This value is extracted from the third case and imposed as mean velocity on the first two cases. For generating the synthetic turbulence in case 2, the mean turbulence intensity (TI) of the rotor plane from case 3 is used as constraint. The Reynolds number for all three cases is $Re_D \approx 63 \cdot 10^6$.

A Dirichlet condition ($\mathbf{U} = \{U_b, 0, 0\}$) at the inlet and a Neumann condition ($\partial\mathbf{U}/\partial\mathbf{n} = 0$) at the sides are chosen as the boundary conditions for the velocity on the first case. For the second case the velocities of the synthetic turbulence field are projected onto the inlet and sides of domain by using a Dirichlet condition. For the third case a precursor simulation is done to obtain a fully developed ABL flow, which is then projected at the inlet of the third case using a Dirichlet condition. The flow of the third case is driven by a pressure gradient inserted as a source term in the momentum equation

$$\frac{F_i}{\rho} = \left\langle \frac{\partial p}{\partial x} \right\rangle = -\frac{u^{*2}}{H + 2D} \tag{12}$$

with the friction velocity $u^* = \sqrt{\tau_w/\rho}$. For the ground velocity a Dirichlet condition ($\mathbf{U} = \mathbf{0}$) is used while the values of $k|_w$ and $\omega|_w$ are defined based on the roughness extension proposed by Knopp *et al.* [18]. For the atmospheric flow this roughness extension can be simplified to

$$k|_{w,\,ABL} = \frac{u^{*2}}{\sqrt{\beta_*}} \qquad \omega|_{w,\,ABL} = \frac{u^*}{\sqrt{\beta_*}\kappa z_0} \tag{13}$$

On the top of the domain a stress free condition and on the sides a Neumann condition ($\partial/\partial\mathbf{n} = 0$) is set for all variables. On the outlet of all three cases a Neumann condition ($\partial/\partial\mathbf{n} = 0$) is imposed.

The spatial resolution in the uniform region around the rotor is chosen to be $\Delta x = D/22$. The actuator line needs a maximum time step of $\Delta x/U_{tip}$ with the tip speed of the rotating blade, which causes the simulations to run on a very low Courant number.

4. Results

In the second case the mean turbulence intensity at rotor position, so $2D$ after the inlet, is reduced by about 14% relative to the reference value from the synthetic field, which can be attributed to dissipation effects inside the computational domain. Another parameter to validate is the integral time scale $\mathcal{T}$. To determine $\mathcal{T}$ the autocorrelation ρ of the time-serie of the streamwise velocity fluctuations is analyzed. $\mathcal{T}$ is determined where $\rho(t = \mathcal{T})$ equals $1/e$ as shown in Figure 3. As both curves almost intersect at that point, the integral time scale with respect to one longitudinal flow-through-time $\mathcal{T}/T$ is found to be around 0.047 with $T = L_x/U_b$ as the longitudinal flow-through-time and with L_x as the domain length. The integral length scale $\mathcal{L}$ in respect to the rotor diameter D is therefore $\mathcal{L}/D = 0.37$. This integral scale is confirmed by looking at the energy spectra of the synthetic and simulated field as shown in Figure 4 where it is close to the maximum of the spectra $f \cdot F_{uu}$. By the same method an integral time scale of $\mathcal{T}/T = 0.036$ and an integral length scale of $\mathcal{L}/D = 0.30$ is obtained at the highest tip point in the rotor plane of the ABL flow.

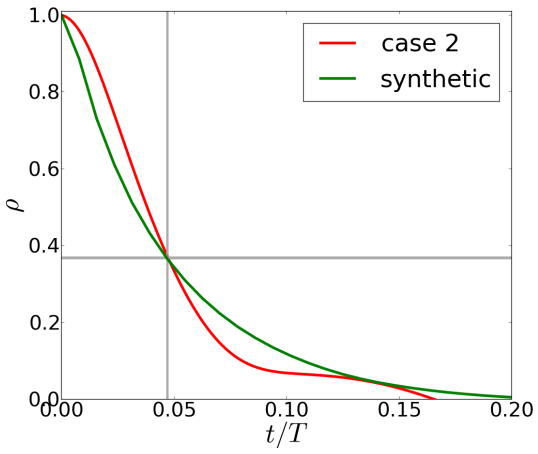

Figure 3. Autocorrelation function of the streamwise velocity fluctuation u with grey lines intersecting at $(\mathcal{T}, 1/e)$

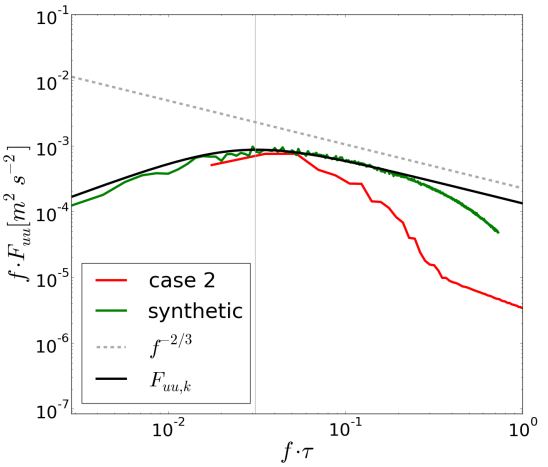

Figure 4. Energy spectrum of streamwise velocity component u with grey solid line indicating $\tau/\mathcal{T}$

In the CFD cases the time series for u are obtained by taking the velocity at fixed points in the rotor and averaging the resulting spectra and autocorrelation functions. In the case of the synthetic field, the wavenumber was transformed to a frequency by the help of the mean bulk velocity U_b, so that $f = k \cdot U_b/(2\pi)$. As the velocities of synthetic field are cyclic [6] the Bartlett method [19] is used for generating the energy spectrum. As this assumption is not valid for the velocity time series of the simulations, the Welch method [20] is applied in these cases.

In Figure 4 it can be seen, that the synthetic velocity field matches well the analytic expression of Equation (5) apart from the higher frequencies. When comparing these spectra to the

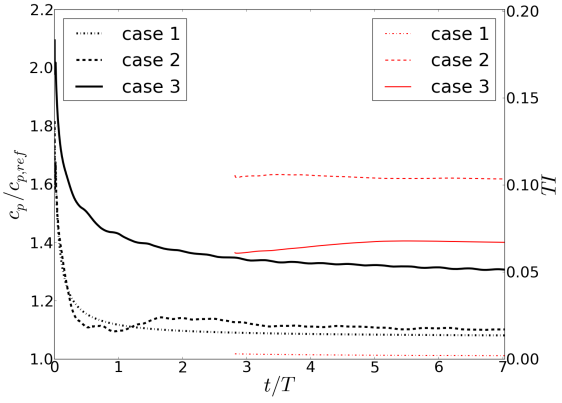

Figure 5. Convergence of normalized power coefficient $c_p/c_{p,ref}$ (black) and turbulence intensity TI (red).

simulated one in case 2, it can be seen that there is a high dissipation, which causes the energy spectrum to drop earlier than expected. In order to circumvent this, a higher spatial resolution, different discretization schemes or different subfilter models could be used. In order to validate the LES also the inertial range is shown as a trend in Figure 4 by the expression $f^{-2/3}$. It can be seen that the simulated spectrum follows this trend for a certain range of frequencies. By refining the mesh it is expected that this range would extend towards the higher frequencies. The frequency on the abscissa is scaled by τ which is linked to the smallest eddy that can be resolved on the computational grid due to the Nyquist-Shannon sampling theorem, so $\tau = 2\Delta x/U_b$.

The total simulation time for each cases is around seven flow-through-times T in order to let the flow reach statistical stationarity. In Figure 5 the development of the mean power coefficient c_p normalized by its reference value $c_{p,ref}$ [3] and the turbulence intensity $TI = \sqrt{2k_{res}}/\langle\overline{U}\rangle$ with $k_{res} = 0.5\langle\overline{u_i}\,\overline{u_i}\rangle$ over the runtime are shown. The calculation of the second order statistics is started later during runtime as first the mean velocity $\langle\overline{U}\rangle$ has to converge. In Figure 5 it can be seen that the power coefficients for the first two cases converge towards a similar value, which can be attributed to the blockage effect as the transversal domain length is $4D$. By extending the domain size, the simulated power coefficients approach the reference value. In case 3 the wake expansion is even more obstructed by the vicinity of the ground and therefore a c_p much higher than the reference value is obtained. When looking at the turbulence intensities it can be seen that they are also reaching convergence in an oscillating manner. It should be noted, that the turbulence intensities are not the same for the second and third case as their calculation is based on the total k_{res} of the whole domain with the presence of a rotor.

When comparing the amount of turbulent kinetic energy of the subfilter scales k_{SGS} and the resolved turbulent kinetic k_{res} energy of the resolved scales, it can be found that more than 90% of the turbulent kinetic energy is resolved for case 2. For case 3 it is a bit more complicated, as in the RANS part in the lower region of the computational domain all turbulent motion is modelled. By excluding this zone from the comparison it can be observed that more than 80% of k is resolved.

In Figure 6 it is shown that the symmetric velocity deficit of the mean streamwise velocity $\langle\overline{U}\rangle$ is almost the same for case 1 and 2 in the vicinity of the rotor, while the deficit in the sheared case is more prominent close to the ground. The wake recovery is quicker in the two turbulent cases as it can be seen in Figure 7.

When looking at the resolved Reynolds stress in Figure 8 it can be seen that fluctuations in case 1 are completely dissipated after a distance of $x/D = 0.5$ behind the rotor. While case 2 exhibits an almost symmetrical profile, there are almost no fluctuations close to the ground in the third case. This can be explained by the fact that the RANS zone of the hybrid model

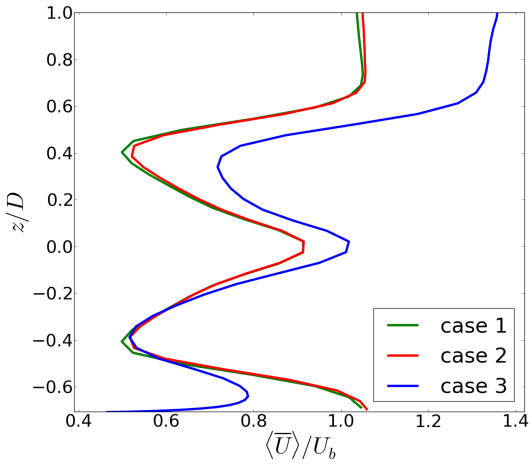

Figure 6. Vertical profile of $\langle\overline{U}\rangle/U_b$ at $x/D = 0.5$ and $y/D = 0$

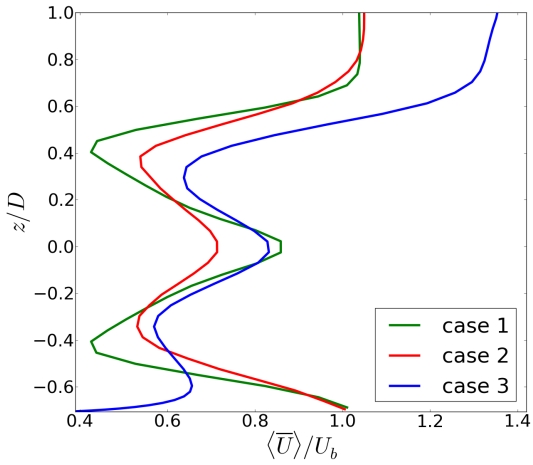

Figure 7. Vertical profile of $\langle\overline{U}\rangle/U_b$ at $x/D = 2.0$ and $y/D = 0$

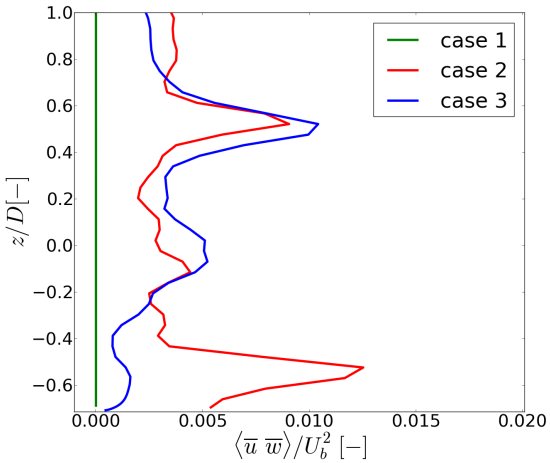

Figure 8. Vertical profile of $\langle\overline{u}\,\overline{u}\rangle/U_b^2$ at $x/D = 0.5$ and $y/D = 0$

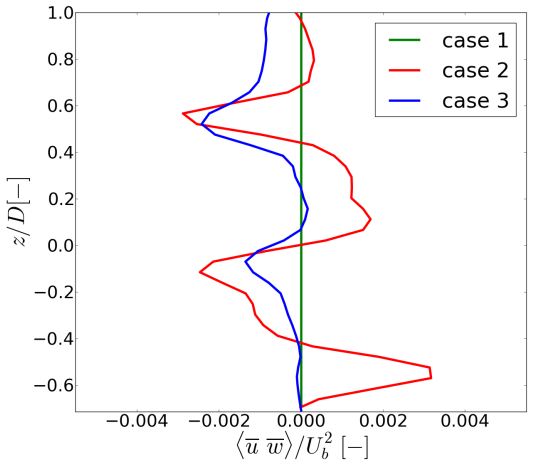

Figure 9. Vertical profile of $\langle\overline{u}\,\overline{w}\rangle/U_b^2$ at $x/D = 0.5$ and $y/D = 0$

reaches into the rotor zone. Therefore, there are almost no resolved fluctuations in this area. A similar behaviour can be observed for the stress $\langle\overline{u}\,\overline{w}\rangle$ in Figure 9. For circumventing this phenomena a higher spatial resolution has to be chosen which would allow the LES zone to expand closer to the ground.

In order to have a look at the vortex dynamics in the near wake, energy spectra are calculated at three different points: in the rotor plane without turbine (Figure 10) and with the turbine (Figure 11), and with the turbine at $0.25D$ (Figure 12) and at $0.5D$ (Figure 13) behind the rotor. In Figure 10 it can be seen that the spectra for case 2 and 3 are very similar although the ABL case exhibits more energy at higher frequencies. The turbulent kinetic energy for the irrotational case is so low, so the energy in the spectrum can be attributed to numerical noise. In Figure 11 a very distinctive energy peak (grey solid line) can be seen at three times the rotating frequency of the three bladed wind turbine, which clearly shows the passage of a rotor

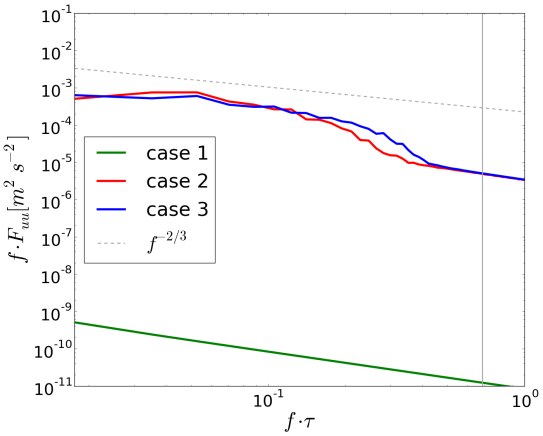

Figure 10. Energy spectrum of u without turbine at $x/D = 0$, $y/D = 0$ and $z/D = 0.5$

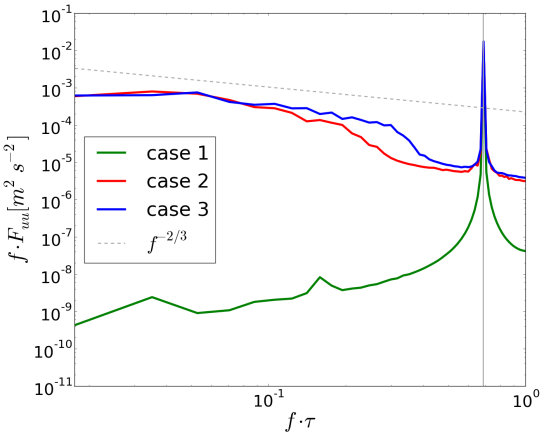

Figure 11. Energy spectrum of u with turbine at $x/D = 0$, $y/D = 0$ and $z/D = 0.5$

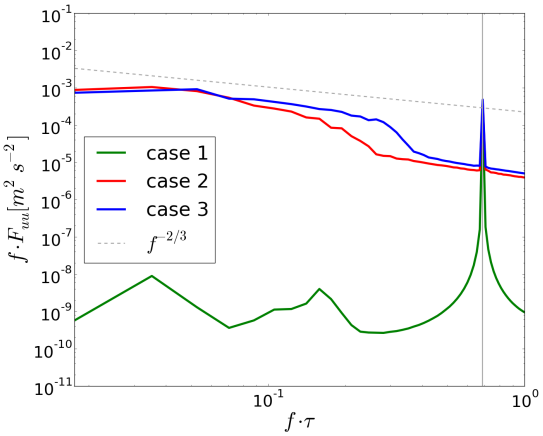

Figure 12. Energy spectrum of u with turbine at $x/D = 0.25$, $y/D = 0$ and $z/D = 0.5$

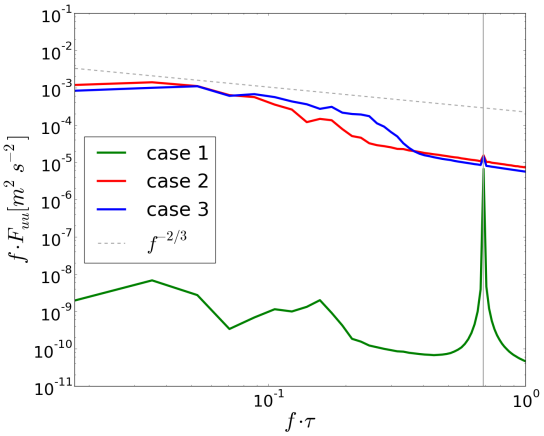

Figure 13. Energy spectrum of u with turbine at $x/D = 0.5$, $y/D = 0$ and $z/D = 0.5$

tip. Further downstream in Figure 12, the energy diminishes while at $0.5D$ in Figure 13 the energy at the frequency of the blade passage is almost zero.

5. Conclusion

The comparison study of the near wake of an actuator line immersed in three different flow situations has been carried out. A crucial aspect was to maintain a certain similarity between the different cases: irrotational flow, homogenous isotropic turbulent flow and an ABL flow. Therefore all three cases exhibit the same mean bulk velocity in the rotor plane, while the two turbulent cases 2 and 3, have also the same mean bulk turbulence intensity.

The simulated homogenous isotropic turbulence (case 2) shows a good agreement with the generated synthetic field with respect to its turbulence intensity and integral length scale of the flow at the rotor position. Hence the method of imposing the generated synthetic field as a boundary condition of the CFD simulation proves to be a valid option for modeling this kind of flow.

The hybrid RANS-LES model reproduces well the sheared turbulence of an ABL flow.

Therefore the vertical profiles of the mean streamwise velocity deficit downstream of the rotor exhibits a strong asymmetry. This is one of the main differences between this case and the two ideal cases which yield symmetric profiles. However the Reynolds stresses for the turbulent cases show a certain similarity far away from the ground. There is a weaker resemblance close to the ground due to the RANS region in the third case.

The energy spectra shows a very good agreement between the turbulent cases 2 and 3. Meanwhile the level of the turbulent kinetic energy of the irrotational flow is not much greater than the numerical noise. When introducing the turbine in the flow a distinctive high energy peak at three times the rotor frequency appears representing the induced velocity field by the blades. This peak diminishes after only half a rotor diameter.

A finer grid would improve the resolution of the tip vortices and turbulence structures and would probably push the RANS zone further away from the rotor plane in case 3.

Acknowledgments

The numerical simulations were performed on the Guillimin and Colosse supercomputer managed by Calcul Québec and Compute Canada. These supercomputer are funded by the Canada Foundation for Innovation (CFI), NanoQuébec, RMGA and *the Fonds de recherche du Québec - Nature et technologies* (FRQ-NT). The research was founded by the *Laboratoire de recherche sur l'aérodynamic des éoliennes en milieu nordique* (AEMN), the *Fonds de recherche du Québec - Nature et technologies* (FRQ-NT), Hydro-Québec, and the Natural Sciences, and Engineering Research Council of Canada (NSERC). Their support is greatly appreciated. We also want to present our gratitude to our colleagues Yann-Äel Muller and Hugo Olivares-Espinosa who assisted us in our efforts for introducing the homogeneous isotropic turbulence for case 2.

References

[1] Vermeer L, Sørensen J and Crespo A 2003 *Progress in Aerospace Sciences* **39** 467–510
[2] Sanderse B 2011 *Wind Energy* **14** 799–819
[3] Jonkman J, Butterfield S, Musial W and Scott G 2009 Definition of a 5-MW reference wind turbine for offshore system development Tech. rep. National Renewable Energy Laboratory
[4] Sørensen J N and Shen W Z 2002 *Journal of Fluids Engineering* **124** 393
[5] Troldborg N 2008 *Actuator Line Modeling of Wind Turbine Wakes PhD thesis* Ph.D. thesis Technical University of Denmark
[6] Mann J 1998 *Probabilistic Engineering Mechanics* **13** 269–282
[7] Olivares-Espinosa H, Breton S P, Nilsson K, Masson C, Dufresne L and Ivanell S 2013 *ICOWES 2013*
[8] Bechmann A 2006 *Large-eddy simulation of atmospheric flow over complex terrain* Ph.D. thesis Risø National Laboratory. Technical University of Denmark risø-PhD-28(EN)
[9] Menter F, Kuntz M and Langtry R 2003 *Turbulence, Heat and Mass Transfer 4* **4** 625–632
[10] Gritskevich M S, Garbaruk A V, Schütze J and Menter F R 2012 *Flow, Turbulence and Combustion* **88** 431–449
[11] Boudreault L E 2011 *Modélisation numérique de la séparation de l'écoulement atmosphérique* Masters's thesis École de Technologie Supérieure
[12] Travin A, Shur M, Strelets M and Spalart P 2002 *Advances in LES of Complex Flows Conference Proceedings* (KluwerAcademic Publishers) pp 239–254
[13] Spalart *et al* P R 1997 *Proceedings of first AFOSR international conference on DNS/LES* (Louisiana Tech University)
[14] Spalart P R, Deck S, Shur M, Squires K, Strelets M and Travin A 2006 *Theoretical and Computational Fluid Dynamics* **20** 181–195
[15] Nikitin N V, Nicoud F, Wasistho B, Squires K D and Spalart P R 2000 *Physics of Fluids* **12** 1629–1632
[16] Shur M L, Spalart P, Strelets M K and Travin A K 2008 *International Journal of Heat and Fluid Flow* **29** 1638–1649
[17] Martínez-Tossas L A, Churchfield M J and Leonardi S 2014 *Wind Energy*
[18] Knopp T, Eisfeld B and Calvo J B 2009 *International Journal of Heat and Fluid Flow* **30** 54–65
[19] Bartlett M S 1948 *Nature* **161** 686–687
[20] Welch P D 1967 *IEEE Transactions on Auio and Electroacoustics* **AU-15** 70–73